Applied Composite Materials
https://doi.org/10.1007/s10443-025-10315-7

RESEARCH

Drop-Weight Impact of Composite Laminates: Modelling the Effect of a Round-Nosed Versus a Flat-Ended Impactor

Yuzhe Ding[1,2] · Michael S. Johnson[2] · Jun Liu[1] · James Dear[1] · Jiaqi Li[1] · Haibao Liu[3] · Anthony J. Kinloch[1] · John P. Dear[1]

Received: 6 November 2024 / Accepted: 5 February 2025
© The Author(s) 2025, corrected publication 2025

Abstract
The present study investigates the effect of the impactor geometry on the impact performance, at relatively high impact energies, of carbon fibre-reinforced polymer (CFRP) laminates with a cross-ply configuration of $[0_2/90_2]$, which were manufactured using unidirectional (UD) carbon-fibre epoxy-matrix plies. Drop-weight impact tests were performed using both round-nosed and flat-ended rigid impactors. White light interferometry (WLI), ultrasonic C-scan and scanning electron microscopy (SEM) were employed to assess the relationship between the indentation profile, the delamination footprint and the fracture morphology along the fracture plane. This study focusses on the coupling between the extent of indentation, the loading responses and the associated damage caused in the CFRP. This damage involved both intralaminar damage, including matrix cracking and fibre-kinking and fracture, and interlaminar, i.e. delamination, damage. This paper studies in more detail the finding that the flat-ended impactor only caused significant damage to the CFRP panel when an impact energy of 25 J and above was attained, which was previously observed by Y. Ding. J. Liu, Z.E.C. Hall. R.A. Brooks, H. Liu, A.J. Kinloch and J.P. Dear, "Damage and energy absorption behaviour of composite laminates under impact loading using different impactor geometries", Composite Structures **321** (2023) 117259. At an impact energy of 25 J, a compressive kink-band fracture plane occurred around the periphery of the flat-ended impactor near the front surface of the laminate. A previously published numerical model has been extended to account for these experimental observations. The modelling accurately predicts the damage features observed for the two types of impactor geometry with indentation playing a significant role on the threshold for damage and the distribution of damage.

Keywords CFRP laminates · Impact tests · Impactor geometry · Modelling studies

✉ John P. Dear
j.dear@imperial.ac.uk

[1] Department of Mechanical Engineering, Imperial, London SW7 2AZ, UK

[2] Faculty of Engineering, University of Nottingham, NG8 1BB Nottingham, UK

[3] School of Engineering and Materials Science, Queen Mary University of London, E1 4NS London, UK

1 Introduction

Composites materials, such as carbon fibre-reinforced polymer (CFRP) laminates, are attractive for structural components in commercial aircraft due to their good fatigue resistance and weight-saving properties. However, impact with foreign objects, such as tools and runway debris, can lead to structural damage in composite materials and this is still an area of concern. For this reason, the drop-weight impact performance of composites is a well-researched topic [1–13]. These studies have looked at, for example, the effects of impactor shape, panel thickness and lay-up on the perforation resistance and the extent and shape of sub-surface damage. For relatively high velocity impacts, increasing the bluntness of the impactor reduces the likelihood of penetration of the CFRP test panel [4]. For lower velocity impacts, the impactor geometry, support arrangement and response of the composite specimen itself affects the shape of the delamination footprint produced beneath the impacted surface [9, 13].

To demonstrate these effects, Sun and Hallet [13] performed impact tests on a composite stringer-stiffened plate to represent an aircraft structure. Sun and Hallet showed that the damage processes observed in simple flat test panels also occurred in these more representative structural components and that the impact damage could be simulated by their modelling studies. They also showed that the initiation of failure, associated with a load drop, could be predicted on the load-time traces. Now, indentation of the struck surface of the CFRP test panel, caused by the impactor, often acts as an initiation point for cracks, facilitating intralaminar cracking propagation within the matrix, and this can lead to interlaminar damage, i.e. delaminations, between the CFRP plies. Further, at relatively high impact energies, other damage such as fibre-kinking and fibre fracture along a fracture plane in the CFRP panel may may be initiated. Butler et al. [14] have applied analytical modelling techniques to predict the compressive fatigue limit of impact damaged composite laminates. In their analytical model, a circular delamination is modelled as a thin film which fits within the central region of barely visible impact damage generated by the impact event. It is also possible to predict the effect on the compressive and fatigue loading on this weakened structure. Their analytical modelling technique was validated by experimental observations.

Numerical simulation plays a pivotal role in understanding the dynamic response and the damage behaviour of composite materials subjected to a low-velocity impact. For example, Zhou et al. [15] have conducted a finite element analysis (FEA) on the low-velocity repeated impact behaviour of composite laminates and showed clearly how the delamination formed at the ply interfaces and its extent depended on the thickness of the panel. Also, Liu et al. [16] have used modelling to replicate the unusual delamination footprint caused by a flat-ended impactor at a relatively low impact energy of 15 Mahesh et al. [17] have studied the impact behaviour of epoxy-matrix composites for different shapes of impactors, e.g. hemispherical, flat-ended and conical, as well as the effect of different thicknesses of composite panel. They showed that a flat-ended impactor produced the most extensive damage followed by the hemispherical impactor. The conical impactor tended to penetrate locally but did not produce very extensive damage. A FEA model has been proposed by Liu et al. [18] which was developed to predict the impact behaviour of CFRP composites using both thermoplastic and thermosetting polymeric matrices and more recently, to study the effect of an impact on CFRP test panels which had been repaired using adhesively-bonded CFRP patches [19]. These FEA simulation approaches (a) model the ply or lamina, as an anisotropic continuum, in

which intralaminar failure can occur and (b) model interlaminar failure, i.e. delaminations, between the plies, using a cohesive, i.e. damage, surface law. These two damage processes are closely coupled and are affected by the shape of the impactor. However, in these modelling studies always a very low impact energy was used, i.e. equal to, or less than, 10.5 J. Hence, no intralaminar fracture plane was induced in the CFRP panel which led to fibre-kinking and fibre fracture being recorded.

Other researchers have used numerical modelling, for example, Palta et al. [20] to study the effect of different frontal profiles for projectile impact on multi-ply flexible fabrics. These fabrics are secured at their edges and the ballistic limits, for a flat-ended cylindrical impactor, conical impactor and spherical impactor, were assessed. The threshold velocity for penetration was lowest for the conical impactor and highest for the flat-ended impactor with the spherical impactor have a threshold between these two extremes. The numerical modelling allowed detail on the transverse displacement contours to be determined, as well as the effects of the weft and warp, in the woven structure. Nilakantan et al. [21] also researched the effect of projectile size and shape on the impact response of a single layer clamped flexible woven fabric using FEA. In their study, the spherical, flat-ended cylindrical and conical impactor had two different sizes. The extent of fabric deformation scaled with the impactor size. Talebi et al. [22] reported a very detailed FEA evaluation on the effect of conical projectiles, with different nose angles, on ballistic penetration of high strength fabrics. This showed clearly how the stress distribution changed markedly with the nose angle and, when the nose tip was blunter, there was a larger punched region.

The present study focuses on the indentation, loading response and associated damage processes, with the aim of providing an enhanced insight into the effects of impactor geometry on the impact performance of a CFRP panel where the impact energy used was 20–25 J. This follows on from a previous experimental study on round-nosed and flat-ended rigid impactors published in [9]. In this paper, a more detailed study of the threshold impact condition for a flat-ended impactor has been performed showing the onset and the nature of the impact damage generated. For comparison, the behaviour at these two impact energies is also explored for a round-nosed impactor. By utilising white light interferometry (WLI), ultrasonic C-scan and scanning electron microscopy (SEM), detailed indentation profiles, delamination footprints and the morphology of any fibre-kinking and fracture, at relatively high impact energies, were obtained. In this paper, the FEA model proposed by Liu et al. [18] has been modified to extend its applicability to the relatively high impact energies used in the present studies. This modelling can reveal in detail the sequence of the different matrix intralaminar failure processes as well as the extent and location of delamination damage, and their relationship to indentation of the upper surface of the CFRP. The novelty of this research is that by employing FEA modelling, it is possible to see in detail the different types of intralaminar and interlaminar damage. These different types of damage, through the thickness of the specimen, are compared for the experiments at an impact energy, when damage is present for round-nosed and flat-ended impactors. Previous research by Ding et al. [9] had shown that the flat-ended impactor only resulted in damage for impact energies of 25 J or over, whilst the round-nosed impactor exhibited damage below this threshold. For this reason, the two impact energies chosen were 20 J when only impact damage using the round-nosed is observed and 25 J when impact damage from using either the round-nosed or the flat-ended impactor is observed. A detailed comparison of damage is undertaken at 25 J for both type of impactors.

2 Experimental Studies

2.1 CFRP Panels

Rectangular CFRP panels with a cross-ply configuration of $[0_2/90_2]_{2s}$ and having a nominal length of 150 mm, a width of 100 mm and a thickness of 4.6 mm were machined from large plaques. These panels were manufactured using a CFRP based on an epoxy-matrix unidirectional prepreg (MTC510-UD300-HS-33%RW from SHD Composites Ltd, UK), containing 60% (volume fraction) of UD T700 carbon fibres. The prepreg plaque was cured via autoclave processing under 6 bars, holding at 110 ℃ for a 120 min dwell time and cooling down at 2℃ per minute.

2.2 Drop-weight Testing

The drop-weight tower (Model 9340 from Instron, UK), as shown in Fig. 1, was employed to conduct the impact tests, following the test requirements of ASTM D7136 [23]. The drop-weight tower was fitted with a data acquisition system that interfaces with a photoelectric sensor, and a load cell capable of measuring up to 22 kN and collecting data at a sampling rate of 500 kHz. Together, these components enable the impact velocity, impact force and displacement at the impact point to be measured. The CFRP panel was supported on steel supports with a 125 mm × 75 mm cut-out window at the lower part of the tower, see Fig. 1, and impacted in the centre by either a round-nosed or flat-ended rigid impactor, see Fig. 2, at impact energy levels of 20 and 25 J. Both impactors were manufactured from stainless steel with a diameter of 16 mm (round-nosed impactor mass: 5.265 kg; flat-ended impactor mass: 5.255 kg) and impact velocities of 2.76 $m.s^{-1}$ and 3.08 $m.s^{-1}$ were employed to achieve impact energies of 20 to 25 J, respectively. At these impact energies of 20 and 25 J, a dropped tool or other high mass impactor travelling at low velocity would produce damage in a composite laminate of thickness 4.6 mm. Before the impact testing was conducted, all the CFRP panels were C-scanned to confirm there were no prior delaminations present. To check the test reproducibility impact tests, using both impactors at both impact energy levels, were repeated and the replicate results for the load-time traces and delamination footprint areas were usually within ± 5% of each other. Load-time traces typically rise to approximately 10 kN and repeat experiments (three in each case) show the load traces usually vary less than 0.5 kN. Likewise, when the delamination area was 1400 mm^2, repeat experiments gave delamination areas within the range 1330 to 1470 mm^2. This was also the case for higher impact energies where the delamination area increased but the variation was ± 5% from the mean.

2.3 Damage Assessment

The present study uses white light interferometry (WLI) to capture the profile of any indentation created by the low-velocity impact, see Fig. 3. This technique employs the principle of Michelson interferometry [24] with phase related interference. As shown in Fig. 3a, a ContourGT 3-D Optical Profilometer (supplied by Bruker, USA) offers a sub-nanoscale resolution and thus is able to give a detailed and accurate surface morphology. The post-impacted panel, with the impact side facing up, was positioned on

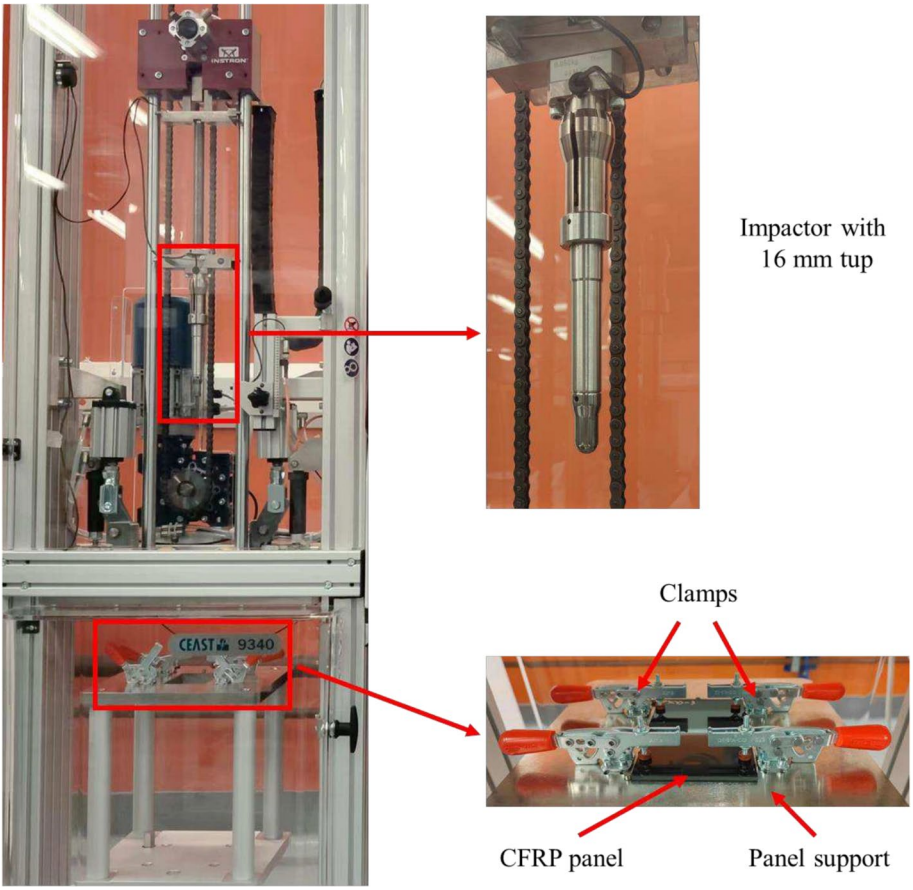


Fig. 1 The drop-weight test set-up equipped with the round-nosed impactor

the sample holder. After establishing the edge of the panel as a reference plane, the probe systematically scanned the target area, dividing it into multiple sub-regions. Upon completion of the scanning, the Bruker Vision software automatically stitched the images from these sub-regions into a 3-D map of the indent. Considering the maximum single scanning area of this profilometer, a rectangular area centred around the impact point with width of 2 mm and length of 40 mm, was selected as the scanned area for WLI scanning only, see Fig. 3b.

After (a) WLI scanning using the profilometer and (b) ultrasonic C-scanning by a portable scanner 'Prisma' (supplied by Sonatest Ltd., UK) all tested panels were cut through the middle line (see Fig. 3b) using a 'Brillant 220' cutting machine (supplied by QATM, Germany) for cross-section inspection under SEM (supplied by TESCAN, Czechia). To reduce the post-impacted panels from damage caused by cutting, a 0.5 mm thick diamond cut-off wheel, having a precision of 1 μm, was used to cut the panels at a forward speed of 0.2 mm per second with a rotational speed of 4000 rpm.

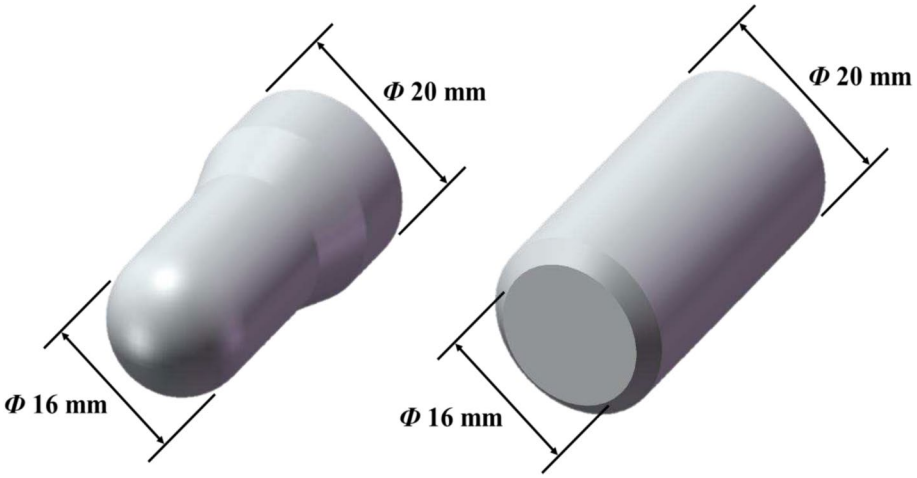


Fig. 2 The round-nosed (left) and flat-ended (right) impactors

3 Numerical Modelling Studies

3.1 Overall Approach

A previous model has been proposed by some of the present authors which simulated very successfully the impact response of continuous CFRP composites based upon thermoplastic and thermosetting matrices [18], and repaired CFRP plates using an adhesively-bonded patch

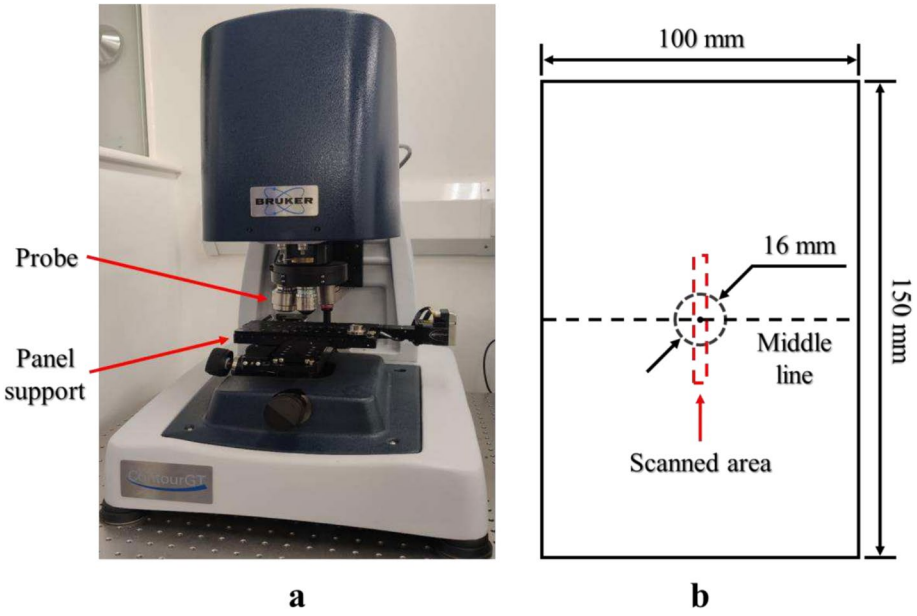


Fig. 3 WLI scanning: **a** ContourGT 3-D Optical Profilometer; **b** Diagram of scanned area (the black dashed circle indicates the impact area)

repair [19], which were subjected to relatively low-velocity impacts of equal to, or less than, 10.5 J. This model [18] is a three-dimensional (3-D) finite-element analysis (FEA) simulation incorporating an elastic-plastic (E-P) damage model and a model for the initiation of intralaminar failure damage based upon the Northwestern University failure criterion [25–27]. These damage models were both implemented as a user-defined material ('VUMAT') sub-routine in a FEA code (in 'Abaqus/Explicit'). However, in these previous tests, at a relatively low impact energy (less than 10.5 J) no major intralaminar fracture plane was observed to result in the CFRP test panel from the impact strike. Such a fracture, which typically occurs at relatively higher impact energies (e.g. 20 and 25 J), as used in the present study, arises from angled intralaminar crack growth in the matrix which causes fibre-kinking, and possibly fibre fracture, along this fracture plane. Indeed, in this previous model [18] the Northwestern University failure criterion was adopted to model the initiation of intralaminar failure which specially excludes the prediction of the initiation of such an intralaminar fracture plane and subsequent fibre damage.

Now, at relatively higher impact energies (i.e. 20 and 25 J), as used in the present study, it is often important to consider the initiation of intralaminar crack growth to give an angled fracture plane. These processes are usually associated with a localised compressive failure. Indeed, such a failure mode has been observed [9] previously in the present CFRP material at relatively high impact energies. When such a fracture plane and associated fibre compressive kink-bands occur they do so in an inclined fracture plane at an angle, θ, to the normal to the ply, which is also normal to the laminate surface. This has been shown experimentally by Ding et al. [9] and previously analysed in detail by many researchers [28–30] typically using the Hashin-Puck criterion [31–35] for the initiation of intralaminar failure. Thus, in the present extended model, the Northwestern University failure criterion [25–27] for the initiation of intralaminar failure used in [18] has been replaced by the equations given in the Hashin-Puck criterion [31–35], since this criterion does model the initiation of an angled intralaminar fracture plane in the matrix, which causes fibre-kinking and may possibly lead to fibre fracture along this fracture plane. Also, the need in the previous work [18] to model a CFRP which was based upon a relatively tough and ductile thermoplastic matrix, i.e. poly(ether-ether ketone), demanded the adoption of an elastic-plastic (E-P) damage model, which is not required for the relatively brittle epoxy matrix employed in the present study. Therefore, to simplify and decrease the run-time of the present model, only an elastic analysis was undertaken.

The implementation of the present model, which has been extended as described above, is shown schematically in Fig. 4, where the overall flowchart for one computational time-step and a single integration point is given. Both the flowcharts for the main model and for the new user-defined sub-routine are shown. As noted above, this present model is based upon the previous model [18] and, for brevity and to avoid repetition, all the methodologies and equations that are used in the numerical model, as given in Fig. 4, are derived and presented in [18]; where the equations are numbered as in Fig. 4. However, as shown in Fig. 4, the Northwestern University failure criterion for the initiation of intralaminar failure used in [18] has been replaced by the equations which are given in the Hashin-Puck criterion [31–35], see below in Table 1. Further, as noted above, only an elastic analysis is undertaken, again see Fig. 4.

It became apparent in this study that the Hashin-Puck criterion, with its inclined intralaminar fracture plane and associated fibre compressive kink-bands, was needed particularly to model accurately the damage around the edge of the flat-ended impactor and for this reason the Hashin-Puck damage criterion was adopted and this will be demonstrated later.

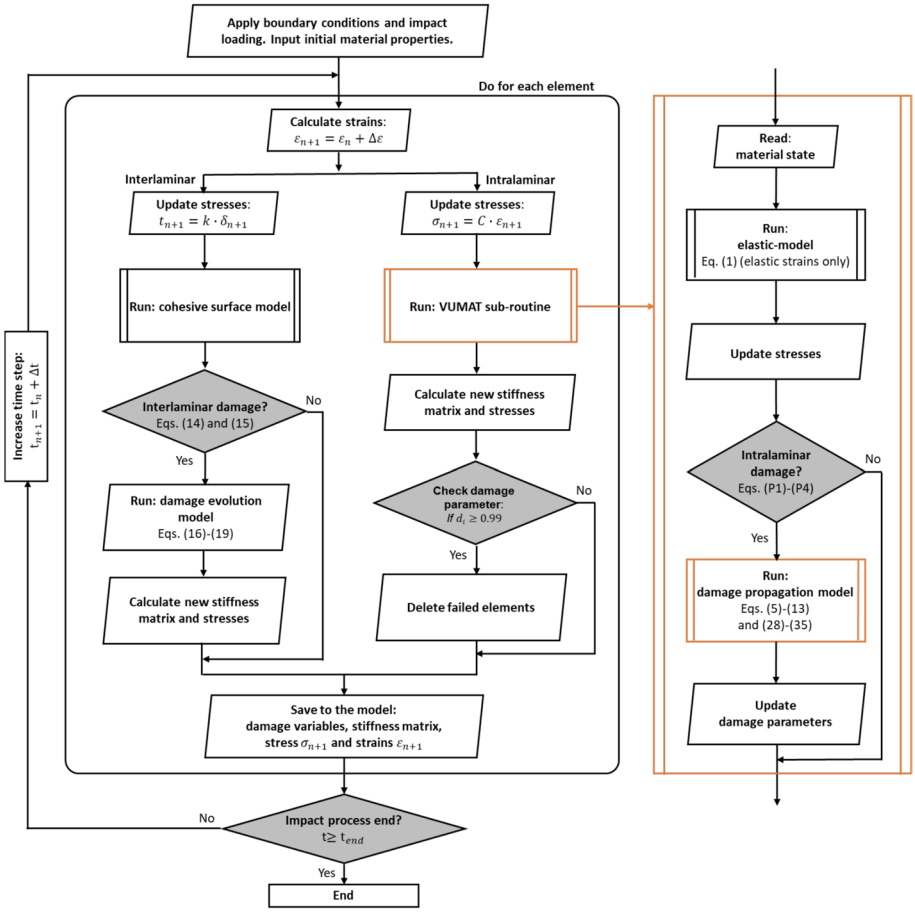


Fig. 4 The implementation of the 3-D FEA model showing schematically the overall flowchart for one computational time-step and a single integration point. Both the flowcharts for the main model and for the user-defined sub-routine are shown. This FEA modelling simulation of the impact event would be run typically over a time-scale, t, of 0 to ca. 6 ms, with ca. 200 time-steps being employed. The simulation runs were stopped when the defined total computation time for the impact simulation event had expired. (All the methodologies and equations that are used in the above FEA model are derived and presented in [18] where they are numbered as in the above figure. Apart from the use of the Hashin-Puck criterion defined by equations P1 to P4 in order to accommodate the damage modes seen at relatively high impact energies as in Table 1.)

3.2 Intralaminar Failure

For the reasons discussed above, to model the initiation of intralaminar failure in the present tests the Hashin-Puck failure criterion [31–35] was employed in a new user-defined material ('VUMAT') sub-routine embedded in the FEA code previously proposed [18], instead of the Northwestern University failure criterion [25–27], see Fig. 4.

The Hashin criterion [32, 33] is widely used for tensile and compressive fibre failure, see Equations (P1) and (P2) in Table 1, as it is efficient in terms of computational time [2, 3, 15,

Table 1 Hashin-Puck criterion for the initiation of intralaminar damage [32–45]

Failure mode	Failure criterion	
Fibre tension $(\sigma_{11} > 0)$	$F_{ft} = \left(\frac{\sigma_{11}}{S_{1t}}\right)^2 + \left(\frac{\sigma_{12}}{S_{12}}\right)^2 + \left(\frac{\sigma_{13}}{S_{13}}\right)^2 \geq 1$	(P1)
Fibre compression $(\sigma_{11} < 0)$	$F_{fc} = \left(\frac{\sigma_{11}}{S_{1c}}\right)^2 \geq 1$	(P2)
Matrix tension $(\sigma_{nn} > 0)$	$F_{mt} = \left(\frac{\sigma_{nn}}{S_{2t}}\right)^2 + \left(\frac{\sigma_{nl}}{S_{12}}\right)^2 + \left(\frac{\sigma_{nt}}{S_{23}^A}\right)^2 \geq 1$	(P3)
Matrix compression $(\sigma_{nn} < 0)$	$F_{mc} = \left(\frac{\sigma_{nt}}{S_{23}^A - \mu_{nt}\sigma_{nn}}\right)^2 + \left(\frac{\sigma_{nl}}{S_{12} - \mu_{nl}\sigma_{nn}}\right)^2 \geq 1$	(P4)
Where:		
$\sigma_{nn} = \sigma_{22}\cos^2\theta + \sigma_{33}\sin^2\theta + 2\sigma_{23}\sin\theta\cos\theta$		
$\sigma_{nl} = \sigma_{12}\cos\theta + \sigma_{13}\sin\theta$	$\sigma_{nt} = \sigma_{23}\left(2\cos^2\theta - 1\right) + \left(\sigma_{33} - \sigma_{22}\right)\sin\theta\cos\theta$	
$S_{12} = S_{13} = S_{23}^A \frac{\mu_{nl}}{\mu_{nt}}$	$S_{23}^A = \frac{S_{2c}}{2}\left(\frac{1-\sin\omega}{\cos\omega}\right)$ $\mu_{nt} = \tan\omega$	$\omega = 2\theta - 90°$
And as defined by:		
σ_{ij} : stress components	S_{12}, S_{13} : transverse shear strengths	
S_{1t}, S_{1c}, S_{2t}, S_{2c} : tensile (t) or compressive (c) strengths in the longitudinal (1) or transverse (2) direction		
S_{23}^A : transverse shear strength of the fracture plane		
σ_{nn}, σ_{nl}, σ_{nt} : normal stress acting on the fracture plane and the shear stresses in the longitudinal and transverse directions of the fracture plane		
μ_{nl}, μ_{nt} : frictional coefficients in the longitudinal (1) or transverse direction (t) of the fracture plane based on the Mohr-Coulomb failure theory		

36]. Turning to transverse failure, the Puck methodology assumes a Mohr-Coulomb type of failure for loading transverse to the fibre direction and he developed an underlying theory to analyse intralaminar crack growth which occurs along a given fracture plane and which typically involves kink-banding of the fibres and fibre fracture. This is often referred to as the Puck criterion [34, 35], see Equations (P3) and (P4) in Table 1, where the criteria for matrix loading under both tensile and compressive stresses are given. The failure is assumed to be caused by the normal and shear stresses which are acting upon the fracture plane, i.e. σ_{nn}, σ_{nl} and σ_{nt}, and these may be deduced as shown in Table 1. The angle for the fracture plane, θ, typically falls within the range of 51° to 55° [27, 36–45]. In summary, when matrix tension, i.e. $\sigma_{nn} > 0$, exists then fracture is assumed to initiate according to the quadratic interaction criterion given in Equation (P3) in Table 1. Whereas, a compressive stress, i.e. $\sigma_{nn} < 0$, acting tends to close any crack which impedes the transverse shear fracture. Puck concluded that for $\sigma_{nn} < 0$ the shear stresses, i.e. σ_{nl}, σ_{nt}, have to overcome an additional resistance which increases with $|\sigma_{nn}|$ and he modelled this by introducing two frictional coefficients, i.e. μ_{nl} and μ_{nt},in the longitudinal and transverse directions, respectively, of the fracture plane based on the Mohr-Coulomb failure theory, to give Equation (P4).

The equations used in the extended model from [18] in the present paper using the Hashin-Puck criterion are given in Table 1. Here the sub-scripts i, j = 1,2, 3 (in σ_{ij}, ν_{ij}, E_{ij} and G_{ij}) refer to the fibre (longitudinal), in-plane (transverse) and out-of-plane (normal) directions and the sub-scripts ft, fc, mt, mc (in F) denote fibre tensile, fibre compression, matrix tensile and matrix compression, respectively. In the 3-D FEA model, once one of the damage criteria in Table 1, i.e. $F \geq 1$, is satisfied, the displacement-based linear damage propagation model, as used previously will be triggered to predict the evolution of the intralaminar damage, see Figs. 4 and [18] for details.

3.3 Interlaminar Failure

The interlaminar damage that arises involves the initiation and growth of delaminations between the plies that make up the composite laminate and its modelling is fully described in [18]. Indeed, in [18] the reader can follow the logical development of the numerical model, the failure criteria used and how crack initiation and propagation for interlaminar damage, i.e. delamination, are defined and quantitatively modelled. As a short summary, interlaminar failure was captured using the 'Abaqus' built-in cohesive surface solution, where the traction is a function of the displacement using a bilinear cohesive law for a linear-softening material model. The energy under the bilinear cohesive law was equivalent to the interlaminar fracture energy, G_c. Before the initiation of delamination, the cohesive law possessed linear-elastic behaviour with a stiffness of k_i. Once the interlaminar damage criterion was satisfied the cohesive stiffness was degraded linearly until separation of the interface occurred, i.e. interlaminar cracking occurred, when the traction tended to zero and the maximum failure displacement was now attained. It should be noted that the initiation and growth of any intralaminar damage significantly influenced the extent of interlaminar damage and hence these two damage modes were modelled to be interactive in the 'Abaqus' simulation.

3.4 FEA Modelling

A 3-D FEA progressive damage model, incorporating a user-defined subroutine 'VUMAT' was created in 'Abaqus/Explicit 2022' to predict the impact performance of the CFRP

Table 2 Material properties of a UD ply of the CFRP laminates [19]

Property	Value
Moduli (GPa)	$E_{11} = 115$; $E_{22} = E_{33} = 8.2$ $G_{23} = 3.6$; $G_{12} = G_{13} = 3.6$
Poisson's ratio	$\nu_{23} = 0.34$; $\nu_{12} = \nu_{13} = 0.34$
Strength, S, values (MPa)	$S_{1t} = 2282$; $S_{2t} = S_{3t} = 54$ $S_{1c} = 1067$; $S_{2c} = S_{3c} = 200$ $S_{12} = S_{13} = S_{23} = 99$
Intralaminar ply fracture energies (kJ/m^2)	$G_{Ic}\|_{ft} = 133$; $G_{Ic\|fc} = 40$ $G_{Ic}\|_{mt} = 0.4$; $G_{Ic}\|_{mc} = 1.3$; $G_{IIc}\|_{ms} = 1.3$
Interlaminar ply fracture energies (kJ/m^2)	$G_{Ic} = 0.4$; $G_{IIc} = 1.3$
Benzeggagh–Kenane exponent	$\eta = 1.45$
Cohesive law strengths (MPa)	$t^0_{33} = 43.0$; $t^0_{31} = t^0_{32} = 50.0$
Initial cohesive law stiffness (MPa/mm)	$k_i = 6.4 \times 10^5$

panels under a relatively high impact energy. As noted above, the flow chart used for the present model is given in Fig. 4, which is based on the previous 3-D FEA model [18] but (a) with the failure criterion for the initiation of intralaminar damage changed to the Hashin-Puck criterion, see Table 1, and (b) the CFRP assumed to behave as a linear-elastic material. It should be noted that during the computation any damaged elements were deleted, as described in [18].

Figure 5 illustrates a quarter of the FEA model for simulating the drop-weight impact, in which the sample holder and clamps were constrained to six degrees of freedom to simulate the real boundary conditions of the CFRP panels during the drop-weight test. The impactors, clamps and sample holder were modelled as discrete bodies and only the impactors were allowed to have a translational freedom in the z-direction and assigned an impact velocity in the predefined field, whilst the clamps and sample holder were rigidly fixed. The contacts between the CFRP laminates and the rigid bodies were assumed to be frictional contacts along the tangential direction with a friction coefficient of 0.2 [18]. The CFRP plies were modelled as 3-D deformable parts between which a finite-thickness (i.e. 0.001 mm) eight-node cohesive element layer (COH3-D8) was inserted, and a penalty algorithm with a friction coefficient of 0.25 was set to describe the tangential contact behaviour [18, 19]. Eight-noded linear-reduced integration (C3-D8R) elements with a size of 1 mm × 1 mm × 1 mm were assigned to the composite plies. Mesh sensitivity analysis

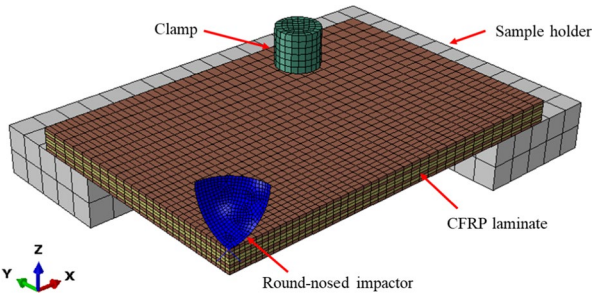


Fig. 5 The quarter configuration of the 3-D FEA model with the round-nosed impactor. (The composites plies are highlighted in brown and khaki for the 0° and 90° fibre orientations, respectively)

studies were performed and it was found that a mesh size of 1 mm x 1 mm x 1 mm gave accurate results for stress and strain gradient and damage evolution in a reasonable time-scale. Typically, the model would take 24 to 30 h to run depending upon the geometry of the impactor. The process for deletion of elements is based on the damage parameter. If the damage parameter exceeds 0.99 then the element is deleted. The material properties of a CFRP UD ply as employed in the model are listed in Table 2.

4 Results and Discussion

4.1 Load-Time Response

Figure 6 presents a comparison between the simulated and experimental load-time response traces at the two impact energies of 20 J and 25 J. At both energy levels, the specimen impacted by either the round-nosed or flat-ended impactor shows oscillatory behaviour on the rising part of the load-time curves. These initial oscillations on the rising part of the load versus time trace are indicative of mass-spring oscillations. These near sinusoidal oscillations in load are mostly affected by the panel elastic stiffness and the masses of the composite panel and the striker, as well as the support arrangement. Contact stiffness at the impact point also plays a significant role. The induced dynamic oscillations decay due to intrinsic damping of the composite panel and frictional effects at the supports [46–49].

It should be noted that there is a significant load drop, for the round-nosed impactor, at approximately 5 kN at 0.8 ms, for both the 20 J and 25 J impacts energies. For the round-nosed impactor, all three repeat load-time traces (i.e. Expts. 1, 2 and 3) are very similar at each impact energy (i.e. 20 and 25 J) and the simulation (the red continuous line) replicates the experimental behaviour very well. For the flat-ended impactor at an impact energy of 20 J, there is no indication of load drop on the rising or falling part of the load-time trace and again the simulation captures this response accurately. Indeed, it will be shown below that no delamination damage was present at this impact energy and this is consistent with no load drop being observed. When the impact energy is increased to 25 J, for the flat-ended impactor, an interesting effect occurs. For Expts. 1 and 2, the load-time trace goes past its maximum value, i.e. just over 12 kN at 2 ms, and then a load drop occurs on the falling part of the curve just under 12 kN. For Expt. 3, at an impact energy of 25 J, there is a load drop just under 12 kN (at 1.4 ms) and this occurs just before the maximum load condition would be expected to be reached. These significant load drops are usually indicative of the initiation of damage [13, 18]. Previous modelling has shown that employing an accurate intralaminar damage model, such as the Hashin-Puck failure criterion for the present tests, is a key factor in predicting these load drops in the load-time trace. For the flat-ended impactor, at an impact energy of 25 J, it is clearly fortuitous that the modelling captures the behaviour of the load drop just before a maximum load of 12 kN would be expected to be reached. Clearly, when the initiation load (just under 12 kN) is nearly coincident with the maximum load condition (just over 12 kN) for the load-time trace there can be an uncertainty, associated with material inhomogeneities or irregularities, as to when damage initiation occurs experimentally and it may now occur on the rising or falling part of the load-time trace. The modelling, on the other hand, will always predict initiation of damage on the rising part of the trace, as this is reached first. This is thought to be the reason why the modelling fortuitously captures the Expt. 3rd case. This variability in response of the damage processes is suggested to be linked to inherent defects in the

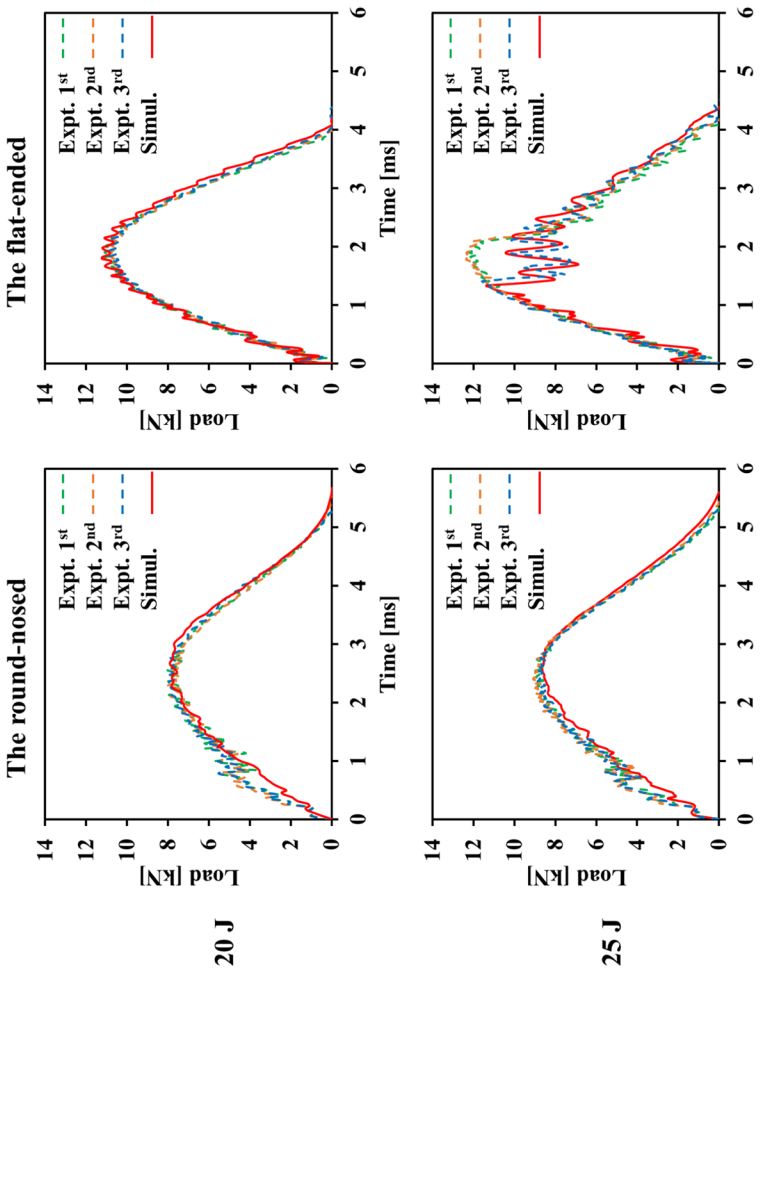


Fig. 6 Load versus time curves from experiments and simulations for the CFRP panels struck by either the round-nosed or the flat-ended impactor at 20 J and 25 J

composite material associated with ply interfaces and related features, and not attributable to the material properties employed in Table 2.

The load-time traces for the round-nosed impactor exhibit a lower peak load and longer contact duration compared with the flat-ended impactor. This is to be expected as the flat-ended impactor is more quickly arrested. At 25 J, the damage initiation load drop at 5 kN for the round-nosed impactor is not quite as dramatic as the damage initiation load drop at just under 12 kN for the flat-ended impactor. When the initiation load for a load drop is higher then more strain energy is stored and the process will be more dramatic. For both types of impactor, these initiation load drops are usually indicative of intralaminar damage followed by interlaminar, i.e. delamination, damage.

4.2 Delamination Damage

The C-scan technique was employed to assess the extent of delamination damage in the CFRP panels. It was found that the shape and extent of the delaminations as predicted from the present 3-D FEA model are very similar to the experimental results, as shown in Fig. 7. These delaminations are colour-coded according to their depth through the CFRP panels. Delaminations nearest the impacted surface give an ultrasonic reflection colour-coded red and delamination furthest from the impact surface gives a reflection colour-coded blue, where dark blue corresponds to a reflection from the rear surface of the specimen. Further, it is evident that the propagation direction of the delamination, at the interface between plies of different direction, exhibits a strong correlation with the fibre orientation of the ply

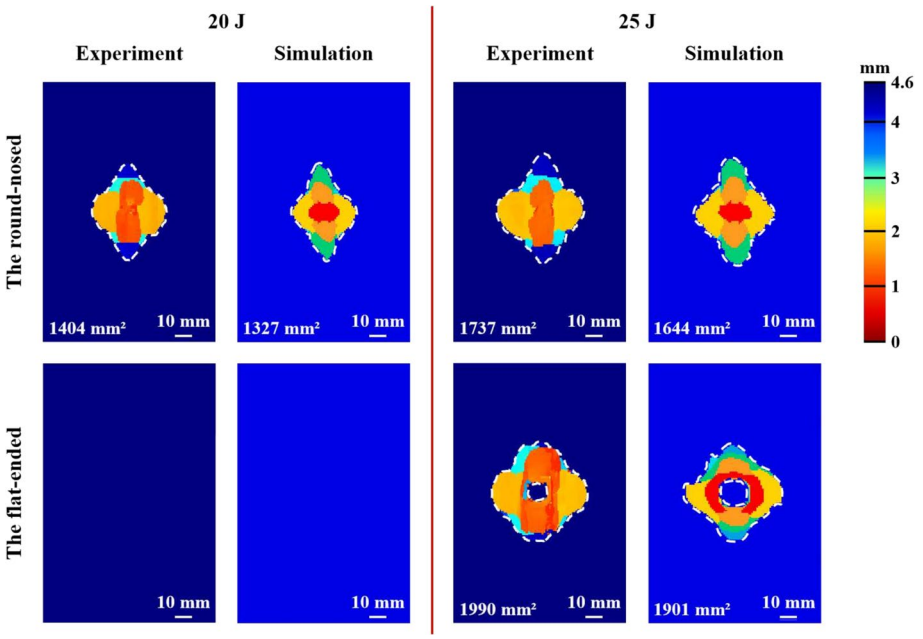


Fig. 7 Delamination footprints (highlighted by the white dashed line) from C-scan experiments [9] and the modelling simulations for the CFRP panels for the round-nosed and the flat-ended impactors at impact energy levels of 20 J and 25 J

below the interface. In the case of the round-nosed impactor, at an impact energy level of 25 J, the delaminations begin at the point of impact and spread outwards in all directions. In contrast, for the flat-ended impactor at 25 J, a circular region, with no delaminations present, corresponding in size to the impactor head, is observed directly beneath the flat-ended impactor. Delaminations then initiate from the edges of this area and propagate outwards towards the boundaries.

It is evident from these experimental and simulation results that the delamination footprint area is approximately 1700 mm^2 for the round-nosed impactor and approximately 2000 mm^2 for the flat-ended impactor at an impact energy of 25 J. Indeed, it is to be expected that a load drop at a higher load, see Fig. 6, would lead to more damage and this is indeed evidenced by the larger delamination footprint for the flat-ended impactor at 25 J. The flat-ended impactor therefore induces a more extensive area of delamination, thus exerting a more detrimental influence on the structural stiffness of the CFRP. It is apparent that the round-nosed impactor is more likely to cause delamination in the CFRP panels. However, once a certain threshold impact energy, i.e. 25 J, is reached, the flat-ended impactor exhibits more significant damage.

A significant observation is that for an impact energy of 20 J, for the round-nosed impactor, there is a load drop around 5 kN at 0.8 ms in Fig. 6 and clear evidence of delamination damage in Fig. 7. However, at the same impact energy of 20 J, for the flat-ended impactor, the load-time trace shows no load drop and there is no evidence of delamination damage. The main difference between the two impactor is that for a round-nosed impactor there is a central localised indentation provided by the round profile. On the other hand, the flat-ended impactor spreads its loading over the frontal area of the impact with no central localised indentation. This indentation process play a very significant part in initiating damage. It is for this reason that the indentation profiles were determined in the next Section.

It should also be noted that, at a high impact energy of 25 J, the delamination area for the flat-ended impactor is more than for a round-nosed impactor with the region directly below the flat-ended impactor showing no delamination. In this study, Compression After Impact (CAI) experiments were not performed, however, it would be expected that the CAI strength would be reduced for a panel struck by the flat-ended impactor at 25 J.

4.3 Indentation Damage

The scanning results from the WLI technique on the post-impacted specimens show clearly the indentation, see Figs. 8 and 9. The characteristic indentation profiles resulting from using the round-nosed and flat-ended impactors were permanently imprinted on the impacted face. For the round-nosed impactor, localised indentation occurs at 20 and 25 J, as shown in Fig. 8. The maximum indentation depth increases from approximately 150 μm at 20 J to 180 μm at 25 J. (It should be noted that the vertical scale is exaggerated compared to the horizontal scale.) For a round-nosed impactor test, the indentation deformation is localised directly under the centre of the impactor. On the other hand, as shown in Fig. 9, the flat-ended impactor induced very little permanent deformation in the material, in the central region, at the 20 J impact energy level. There was a minor resin squeeze-out of the order of 30 μm, at the periphery of the impact zone, for the 20 J impact energy. As the cured ply thickness is approximately 575 μm, it is possible for there to be some fibre damage but it will be a very small fraction of the cured ply thickness. For this reason, it seems reasonable to neglect the minor change in mechanical performance due to this squeeze out effect. With a further increase to an impact energy of 25 J, the indentation became particularly pronounced with a depth of approximately

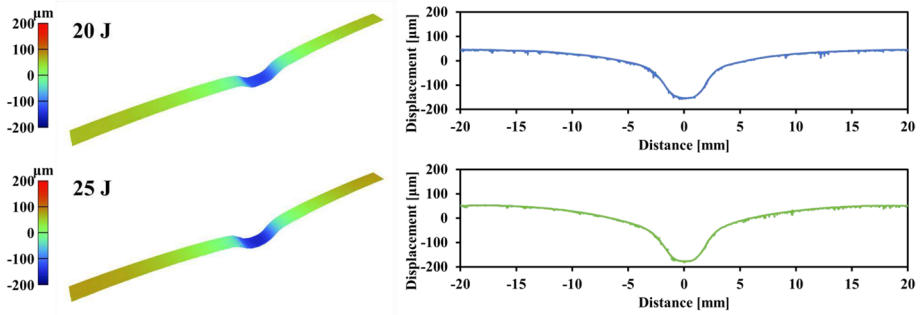


Fig. 8 WLI scanning results of the indentation induced by the round-nosed impactor at impact energies of 20 and 25 J and corresponding displacement curves along the centreline of the selected area, see Fig. 3b. (Please note that the vertical scale is exaggerated compared to horizontal scale.)

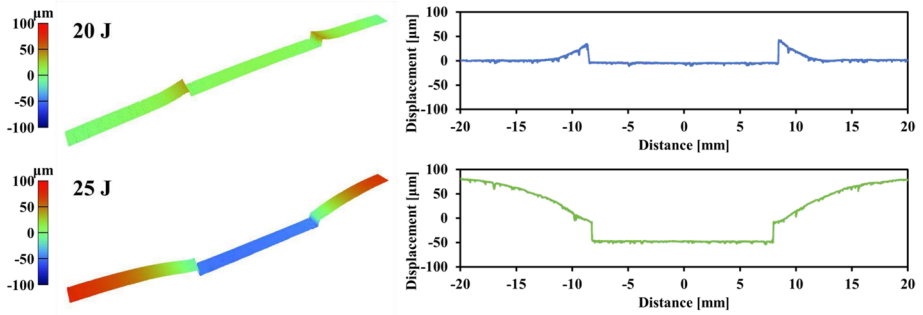


Fig. 9 WLI scanning results of the indentation induced by the flat-ended impactor at impact energies of 20 and 25 J and corresponding displacement curves along the centreline of the selected area, see Fig. 3b. (Please note that the vertical scale is exaggerated compared to horizontal scale.)

50 µm being measured, accompanied by a severe material bulge in the surrounding area. There is a distinct step at the edge of the contact area indicating some sub-surface movement of the facing ply. The indications are that this indentation is linked to the shape of the delamination damage observed for the flat-ended impactor at 25 J, as shown in Fig. 7. It is evident that the indentations caused by the flat-ended impactor exhibit a cylindrical geometry, which is very distinct from the very localised central damage generated by the round-nosed impactor. For the round-nosed impactor, the contact area grows from a point contact to a circular zone as the material deforms under the incoming round-nosed impactor. This results in a significant stress concentration arising under the impactor tip. This leads to disruption and damage in the matrix of the facing ply. In contrast, the flat-ended impactor maintains a planar contact with the CFRP panel throughout the impact event. This leads to a substantial reduction of the transverse shear stress, thereby preventing the formation of indentations at lower energy levels. However, due to its larger contact area, once the applied stress reaches the shear strength of the material, an instantaneous and extensive indentation is formed.

4.4 Morphology of the Intralaminar Fracture Plane

To understand better the damage processes that occurred in the intralaminar fracture plane, sections were cut transversely through the middle line (see Fig. 3b) for cross-section

inspection. It was found that the impactor geometry directly influences the characteristics of the fibre fracture that results at high impact energies of 25 J. That is with matrix tensile cracking and associated fibre full-out fracture at the lower plies occurring for the round-nosed impactor and matrix compressive cracking and associated fibre-kinking fracture occurring at the upper plies for the flat-ended impactor, as shown in Fig. 10. During the round-nosed impact, the gradually increasing contact area results in a stress propagating normal to the growing contact surface, preventing excessive transverse shear stresses. As a consequence, the CFRP material matrix directly under the round-nosed impactor undergoes compressive deformation, and the panel experiences bending deformation in the through-thickness direction. This results in the lowest ply, on the non-impacted side, experiencing the maximum tensile stress and associated longitudinal strain. This is where fibre tensile failure will occur, once its longitudinal tensile strength is reached. For the flat-ended impactor, a larger planar surface and sustained planar contact with the specimen, mitigates the stress concentration with the structural bending deformation oriented to the through-thickness direction. When the compressive strength, due to localised compression and shear loading of the matrix and associated fibres is exceeded, the uppermost plies of the CFRP are the first to experience fibre-kinking fracture with flat and sharp fractured fibre heads. Under the combined influence of structural bending deformation, a kink-band fracture plane with a specific angle of 55° was formed for an impact energy level of 25 J. This corresponds with the orientation of the fracture plane associated with the compressive kink band which is a feature of the Hashin-Puck failure criterion. Repeat experiments showed consistent behaviour with fibre full-out fracture at the lower plies occurring for the round-nosed impactor, beneath the centre of the impactor and fibre-kinking fracture occurring at the upper plies for the flat-ended impactor, near the edge of the flat-ended impactor. These observations agree with previous results [9] and confirm that to model accurately the

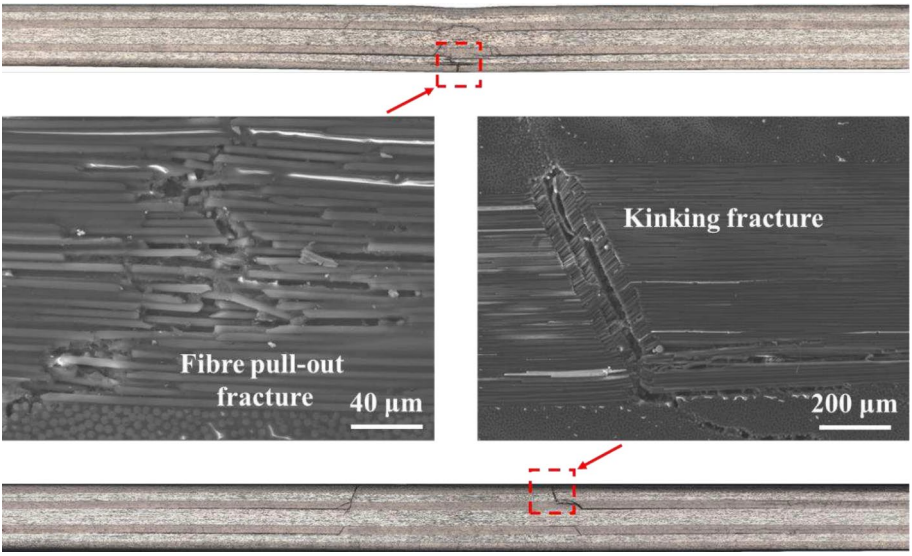


Fig. 10 Optical and SEM micrographs of the cross-section of the round-nosed (top and left) and the flat-ended (bottom and right) impacted CFRP panels at an energy level of 25 J showing fibre pull-out fracture (left) of the lower plies from the round-nosed impactor and fibre-kinking and fibre fracture (right) of the upper plies from the flat-ended impactor [9]

present results at 20 J and 25 J impact energies the use of the Hashin-Puck failure criterion should be adopted, as in the present extended model.

4.5 Numerical 3-D FEA Results for Indentation and Matrix Intralaminar Damage

The delamination predictions from the extended 3-D FEA model, i.e. with the Hashin-Puck failure criterion, for round-nosed and flat-ended impactors were shown earlier in Sect. 4.2 for impact energies of 20 and 25 J. In the present section this extended 3-D FEA model has been employed to analyse the indentation and intralaminar matrix damage processes for the round-nosed and flat-ended impactor at an impact energy of 25 J. Thus, in Fig. 11 the predicted matrix intralaminar damage under the round-nosed (top) and flat-ended (bottom) impactors at an energy level of 25 J.

In Fig. 11, damage areas are colour coded with blue representing no matrix damage, red representing matrix tensile damage, green representing matrix compressive damage and yellow representing mixed matrix tensile/compressive damage. These matrix damage modes are based on the Hashin-Puck failure criterion, see Table 1. It can be seen that, under the round-nosed impactor, matrix tensile damage (red) occurs first at about 0.5 ms at the lowest ply and then spreads upwards, whilst matrix compressive damage (green) occurs at 1 ms and spreads downwards. At 2 ms, mixed matrix tensile/compressive damage (yellow) occurs and this leads to the central indentation observed experimentally. Hence, in terms of intralaminar failure, the indentation caused by the round-nosed impactor is a combination of matrix tensile and compressive damage. As shown experimentally in Fig. 10 (top and left), this is accompanied by fibre tensile damage (fibre pull-out damage).

However, for the flat-ended impactor, in Fig. 11, matrix tensile damage (red) was the main type of matrix damage observed during the loading stage (at 1.05 ms and later) and this was present mostly in the lower plies. Also, visible is compressive failure (leading to fibre-kinking and fibre fracture), evident as compressive matrix damage (green), which occurred (at about 1.05 ms and later) in the upper plies near the edge of the flat-ended impactor. This is also shown experimentally in Fig. 10 (bottom and right). The flat-ended impactor generates a larger area of bending deformation and as a result more widespread matrix tensile damage. This leads to a stress concentration on the edge of the flat-ended impactor and the mixed tensile/compressive matrix damage (yellow) which occurs at 1.75 ms. Finally, the numerical FEA simulations reveal the round-nosed

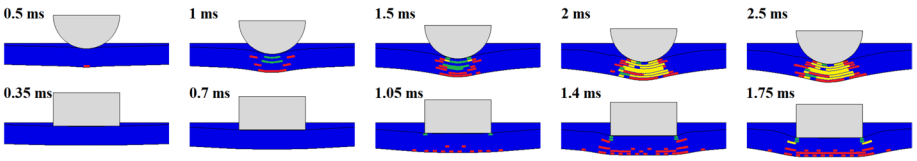


Fig. 11 The predicted matrix intralaminar damage under the round-nosed (top) and flat-ended (bottom) impactors at an energy level of 25 J. (Blue – no damage; red – matrix tensile damage; green - matrix compressive damage and yellow - matrix mixed tensile/compressive damage.) The cross-section shown is across the transverse width of the specimen, i.e. along the middle line in Fig. 3b, and the deflection of the panel is shown along with the matrix intralaminar damage. The blue area is made up of the specimen cross-section (below the impactor) and a view of the top surface (looking back along the length of specimen) – there is a faint black line which delineates the top surface edge of the cross-section and follows a similar profile as the lower surface edge of the cross-section

impactor would indeed be expected to induce more localised central matrix damage compared to the flat-ended impactor, as expected from studying the indentation profiles in Figs. 8 and 9.

To understand better how this intralaminar damage develops under the different shapes of impactor, Fig. 12 shows the magnitude of the maximum stress (tension, compressive or shear) across the cross-sectional thickness, for a round-nosed impactor and for a flat-ended impactor, at an impact energy of 25 J. This maximum stress is shown as it relates most closely to onset of damage. The stress distribution is shown at 2.5 ms for the round-nosed impactor and at 1.4 ms for the flat ended impactor and these times are when appreciable damage occurs for the round-nosed and flat-ended impactors respectively in Fig. 11. The impact of the round-nosed impactor on the upper surface of the composite leads to high tensile stresses on the lower surface directly below the centre of the round-nosed impactor. These tensile stresses result in the matrix tensile failure and associated fibre pull-out fracture, of the lower plies (see Fig. 10, top and left). The stress levels are lower in the central region under the flat-ended impactor but are appreciable around the periphery of the flat-ended impactor, where compression exacerbated by shear, takes place leading to matrix compressive failure and fibre-kinking fracture (see Fig. 10, bottom and right).

Figure 13 shows the stress-strain behaviour near a failure point, during the impact event up to onset of failure, for a round-nosed and a flat-ended impactor, at an impact energy of 25 J. For the round-nosed impactor, the point chosen is on the lower surface directly beneath the centre of the round-nosed impactor (marked with a symbol + on Fig. 12). This tensile stress leads to matrix tensile failure followed by fibre full-out fracture at the lower plies for the round-nosed impactor. For the flat-ended impactor, the point chosen is at the corner of the flat-ended impactor near the upper surface plies (marked with a symbol + on Fig. 12) and the compressive stress is shown which leads to compressive matrix failure followed by fibre-kinking fracture occurring in the upper plies. The maximum values of stress and strain are consistent with the materials properties in Table 2 as to be expected.

Figure 14 shows a comparison, after the impact event, of the indentation profile (or upper surface displacement curve) from WLI scanning (green line) and the modelling simulation (black line) from the extended FEA model, where the blue area is the uppermost ply of the CFRP panel, for an impact energy of 25 J. It may be seen that the simulation generates, with reasonable accuracy, the residual indentation generated by the impact event. Further, it would appear that the indentation profiles are mainly produced by matrix damage and movement of the plies under and near the impact zone. Indeed, there is no material plasticity built into this extended FEA model and all the indentation damage can be attributed to these matrix damage processes.

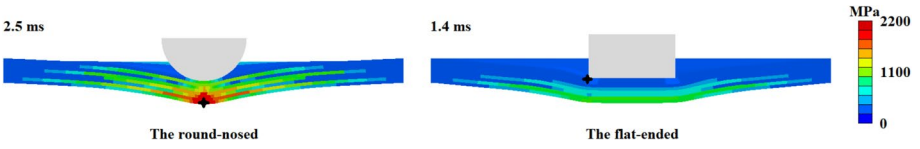


Fig. 12 Magnitude of maximum stress (tension, compression or shear stress, in MPa) over the cross-section across the transverse width of the specimen, at 2.5 ms for the round-nosed impactor (left) and at 1.4 ms for the flat-ended impactor (right). This is for an impact energy of 25 J (The symbol + indicates local high points of stress where failure occurs). The times of 2.5 ms for the round-nosed impactor and 1.4 ms for the flat-ended impactor were chosen as these correspond to when appreciable damage occurs (see Fig. 11)

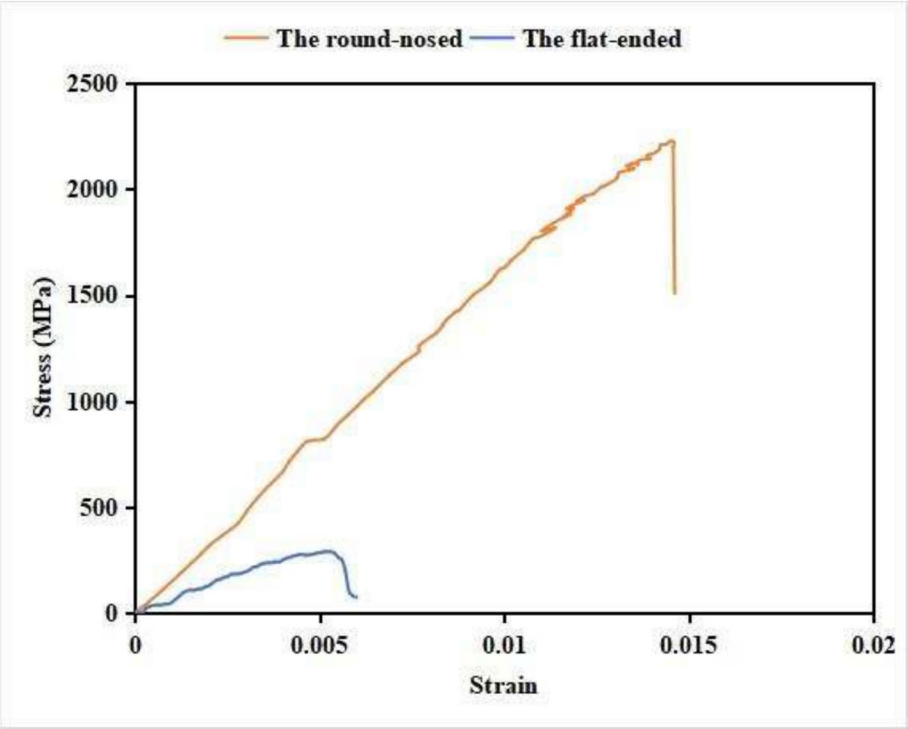


Fig. 13 Stress-strain relationships near failure points (marked with a symbol + on Fig. 12) during the impact event for the round-nosed impactor (brown – tensile stress) and for the flat-ended impactor (blue – compressive stress)

5 Conclusions

The present research has focussed on an experimental and numerical study of the impact loading, at relatively high impact energies of 20 J and 25 J, of a CFRP laminate using either a round-nosed or a flat-ended shape impactor. A previous numerical 3-D FEA model has been extended to model the load-time and damage induced at these relatively high impact energies.

The main findings are:

- The round-nosed impactor is more likely to cause impact damage due to stress concentrations at the impact point and this initiates intralaminar and interlaminar, i.e. delamination, damage.
- The flat-ended impactor spreads the loading over its front circular face and this leads to a higher threshold of impact energy for significant damage of 25 J.
- The impactor geometry has significant effects on the intralaminar failure modes of the CFRP. For the round-nosed impactor, localised matrix tensile and compressive damage occurs under the impactor and drives delamination. At the rear surface of the panel, fibre pull-out can occur at these high impact energies.

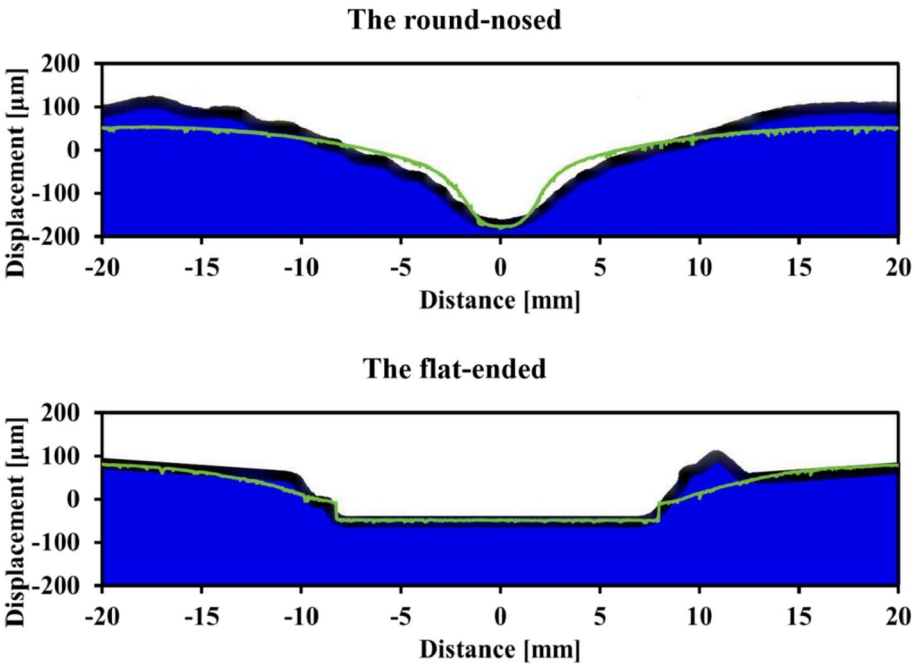


Fig. 14 Comparison of the indentation profiles (upper surface displacement curve) from WLI scanning (green lines) and simulation of upper surface displacement (black line) caused by the round-nosed and flat-ended impactors, where the blue area is the CFRP panel cross-section, for an impact energy of 25 J

- For the flat-ended impactor, matrix tensile failure tends to occur at the rear surface and bending drives delamination. On the front surface, around the periphery of the flat-ended impactor, a fracture plane is created which includes a fibre kink-band and fibre fracture to occur at the relatively high impact energy of 25 J.
- Further, the indentation of the front, impacted, surface of the CFRP for the two types of impactors have different characteristic shapes. The round-nosed impactor induces a more localised but deep indentation of approximately 180 µm at 25 J. The indentation depth for the flat-ended impactor is only approximately 50 µm at 25 J. However, it has a far more distinct shape with a bulge of material in the area surrounding the indentation.
- To model the different damage modes at these relatively high impact energies, a previous 3-D FEA progressive damage model has been extended to include the Hashin-Puck failure criterion for the initiation of intralaminar matrix damage. Since this failure criterion was considered to be an appropriate criterion to capture the damage mode of the formation of a fracture plane with associated fibre-kinking and fibre fracture when the flat-ended impactor was used.
- The 3-D FEA, with Hashin-Puck damage modelling, captures well the differences in damage observed for the round-nosed and flat-ended impactors and clearly indentation plays a very significant part in determining the threshold for onset of damage and the shape of the damage observed.

Acknowledgements The manufacture of composite panels by Professor Lee Harper and Dr. Adam Joesbury, Composites Research Group, University of Nottingham is very much appreciated. For the purpose of open access, the authors have applied a Creative Commons Attribution (CC BY) license to any Author Accepted Manuscript version.

Author Contributions Y.D. wrote the original draft of the manuscript and prepared all figures. A.J.K. and J.P.D. reviewed and edited the manuscript. All authors reviewed the final manuscript and provided useful input to the methodology and associated experimentation and modelling for this research.

Data Availability No datasets were generated or analysed during the current study.

Declarations

Competing Interests The authors declare no competing interests.

Open Access This article is licensed under a Creative Commons Attribution 4.0 International License, which permits use, sharing, adaptation, distribution and reproduction in any medium or format, as long as you give appropriate credit to the original author(s) and the source, provide a link to the Creative Commons licence, and indicate if changes were made. The images or other third party material in this article are included in the article's Creative Commons licence, unless indicated otherwise in a credit line to the material. If material is not included in the article's Creative Commons licence and your intended use is not permitted by statutory regulation or exceeds the permitted use, you will need to obtain permission directly from the copyright holder. To view a copy of this licence, visit http://creativecommons.org/licenses/by/4.0/.

References

1. Andrew, J.J., Srinivasan, S.M., Arockiarajan, A., Dhakal, H.N.: Parameters influencing the impact response of fiber-reinforced polymer matrix composite materials: A critical review. Compos. Struct. **224**, 111007 (2019)
2. Shah, S.Z., Karuppanan, S., Megat-Yusoff, P.S., Sajid, Z.: Impact resistance and damage tolerance of fiber reinforced composites: a review. Compos. Struct. **217**, 100–121 (2019)
3. Bogenfeld, R., Kreikemeier, J., Wille, T.: Review and benchmark study on the analysis of low-velocity impact on composite laminates. Eng. Fail. Anal. **86**, 72–99 (2018)
4. Fan, J., Guan, Z., Cantwell, W.J.: Modeling perforation in glass fiber reinforced composites subjected to low velocity impact loading. Polym. Compos. **32**, 1380–1388 (2011)
5. Mitrevski, T., Marshall, I.H., Thomson, R.: The influence of impactor shape on the damage to composite laminates. Compos. Struct. **76**, 116–122 (2006)
6. Lee, S.M., Cheon, J.S., Im, Y.T.: Experimental and numerical study of the impact behavior of SMC plates. Compos. Struct. **47**, 551–561 (1999)
7. Zhou, G., Lloyd, J.C., McGuirk, J.J.: Experimental evaluation of geometric factors affecting damage mechanisms in carbon/epoxy plates. Compos. Part A: Appl. Sci. Manufac. **32**, 71–84 (2001)
8. Dhakal, H.N., Zhang, Z.Y., Bennett, N., Reis, P.N.: Low-velocity impact response of non-woven hemp fibre reinforced unsaturated polyester composites: Influence of impactor geometry and impact velocity. Compos. Struct. **94**, 2756–2763 (2012)
9. Ding, Y., Liu, J., Hall, Z.E., Brooks, R.A., Liu, H., Kinloch, A.J., Dear, J.P.: Damage and energy absorption behaviour of composite laminates under impact loading using different impactor geometries. Compos. Struct. **321**, 117259 (2023)
10. Icten, B.M., Kıral, B.G., Deniz, M.E.: Impactor diameter effect on low velocity impact response of woven glass epoxy composite plates. Compos. Part. B: Eng. **50**, 325–332 (2013)
11. Zhou, J., Liao, B., Shi, Y., Zuo, Y., Tuo, H., Jia, L.: Low-velocity impact behavior and residual tensile strength of CFRP laminates. Compos. Part. B: Eng. **161**, 300–313 (2019)
12. Sevkat, E., Liaw, B., Delale, F.: Drop-weight impact response of hybrid composites impacted by impactor of various geometries. Mater. Design **52**, 67–77 (2013). ((**1980–2015**))
13. Sun, X.C., Hallett, S.R.: Barely visible impact damage in scaled composite laminates: Experiments and numerical simulations. Int. J. Impact Eng. **109**, 178–195 (2017)
14. Butler, R., Almond, D.P., Hunt, G.W., Hu, B., Gathercole, N.: Compressive fatigue limit of impact damaged composite laminates. Compos. Part A: Appl. Sci. Manufac. **38**, 1211–1215 (2007)

15. Zhou, J., Wen, P., Wang, S.: Finite element analysis of a modified progressive damage model for composite laminates under low-velocity impact. Compos. Struct. **225**, 111113 (2019)
16. Liu, H., Liu, J., Ding, Y., Zhou, J., Kong, X., Blackman, B.R., Kinloch, A.J., Falzon, B.G., Dear, J.P.: Effects of impactor geometry on the low-velocity impact behaviour of fibre-reinforced composites: an experimental and theoretical investigation. Appl. Compos. Mater. **27**, 533–553 (2020)
17. Mahesh, V., Joladarashi, S., Kulkarni, S.M.: Influence of laminate thickness and impactor shape on low velocity impact response of jute-epoxy composite: FE study. Materials Today: Proc. **28**, 545–550 (2020)
18. Liu, H., Liu, J., Ding, Y., Hall, Z.E., Kong, X., Zhou, J., Blackman, B.R., Kinloch, A.J., Dear, J.P.: A three-dimensional elastic-plastic damage model for predicting the impact behaviour of fibre-reinforced polymer-matrix composites. Compos. Part. B: Eng. **201**, 108389 (2020)
19. Liu, H., Liu, J., Hall, Z.E., Brooks, R.A., Crocker, J.W., Joesbury, A.M., Harper, L.T., Blackman, B.R., Kinloch, A.J., Dear, J.P.: Modelling the effects of patch-plug configuration on the impact performance of patch-repaired composite laminates. Compos. Sci. Technol. **233**, 109917 (2023)
20. Palta, E., Fang, H., Weggel, D.C.: A numerical study of the effects of projectile properties on the impact behaviour of multi-ply flexible fabrics. Appl. Compos. Mater. **31**, 511–533 (2024)
21. Nilakantan, G., Wetzel, E.D., Bogetti, T.A., Gillespie, J.W., Jr.: A deterministic finite element analysis of the effects of projectile characteristics on the impact response of fully clamped flexible woven fabrics. Compos. Struct. **95**, 191–201 (2013)
22. Talebi, H., Wong, S.V., Hamouda, A.M.S.: Finite element evaluation of projectile nose angle effects in ballistic perforation of high strength fabric. Compos. Struct. **87**, 314–320 (2009)
23. ASTM D7136: Standard test method for measuring the damage resistance of a fiber-reinforced polymer matrix composite to a drop-weight impact event. ASTM International, Philadelphia, PA (2012)
24. Yang, S., Zhang, G.: A review of interferometry for geometric measurement. Meas. Sci. Technol. **29**, 102001 (2018)
25. Daniel, I.M., Luo, J., Schubel, P.M.: Three-dimensional characterization of textile composites. Compos. Part. B: Eng. **39**, 13–19 (2008)
26. Daniel, I.M., Luo, J., Schubel, P.M., Werner, B.T.: Interfiber/interlaminar failure of composites under multi-axial states of stress. Compos. Sci. Technol. **69**, 764–771 (2009)
27. Daniel, I.M.: Failure of composite materials. Strain **43**, 4–12 (2007)
28. Zheng, J., Maharaj, C., Liu, J., Chai, H., Liu, H.L., Dear, J.P.: A comparative study on the failure criteria for predicting the damage initiation in fiber reinforced composites. Mech. Compos. Mater. **58**, 125–140 (2022)
29. Davies, G.A., Olsson, R.: Impact on composite structures. Aeronaut. J. **108**, 541–563 (2004)
30. Pinho, S.T., Iannucci, L., Robinson, P.: Physically-based failure models and criteria for laminated fibre-reinforced composites with emphasis on fibre-kinking: Part I: Development. Compos. Part A: Appl. Sci. Manufac. **37**, 63–73 (2006)
31. Zhang, D., Zhang, C., Qi, J., Zhou, J., Zheng, X., Liu, H.: Experimental and numerical studies on filled-hole compression of FRP laminates considering different countersunk hole configurations. Constr. Build. Mater. **417**, 135305 (2024)
32. Hashin, Z., Rotem, A.: Fatigue failure criterion for fiber reinforced materials. J. Compos. Mater. **7**, 448–464 (1973)
33. Hashin, Z.: Failure criteria for unidirectional fiber composites. J. Appl. Mech. **47**, 329–334 (1980)
34. Puck, A., Schürmann, H.: Failure analysis of FRP laminates by means of physically based phenomenological models. Compos. Sci. Technol. **62**, 1633–1662 (2002)
35. Deuschle, H.M., Puck, A.: Application of the Puck failure theory for fibre-reinforced composites under three-dimensional stress: Comparison with experimental results. J. Compos. Mater. **47**, 826–846 (2013)
36. Li, X., Ma, D., Liu, H., Tan, W., Gong, X., Zhang, C., Li, Y.: Assessment of failure criteria and damage evolution methods for composite laminates under low-velocity impact. Compos. Struct. **207**, 727–739 (2019)
37. Pinho, S.T., Iannucci, L., Robinson, P.: Physically based failure models and criteria for laminated fibre-reinforced composites with emphasis on fibre-kinking. Part II: FE implementation. Compos. Part A: Appl. Sci. Manufac. **37**, 766–777 (2006)
38. Huang, L., Tao, Y., Sun, J., Zhang, D., Zhao, J.: Assessment of numerical modeling approaches for thin composite laminates under low-velocity impact. Thin-Walled Struct. **191**, 111053 (2023)
39. Rezasefat, M., Gonzalez-Jimenez, A., Giglio, M., Manes, A.: Numerical study on the dynamic progressive failure due to low-velocity repeated impacts in thin CFRP laminated composite plates. Thin-Walled Struct. **167**, 108220 (2021)

40. Mohammed, M.A., Tarfaoui, M.: A progressive damage modelling of glass/epoxy cylindrical structure subjected to low-velocity impact. Eng. Fail. Anal. **134**, 106036 (2022)
41. Wiegand, J., Petrinic, N., Elliott, B.: An algorithm for determination of the fracture angle for the three-dimensional Puck matrix failure criterion for UD composites. Compos. Sci. Technol. **68**, 2511–2517 (2008)
42. Falzon, B.G., Apruzzese, P.: Numerical analysis of intralaminar failure mechanisms in composite structures. Part I: FE implementation. Compos. Struct. **93**, 1039–1046 (2011)
43. Tan, W., Falzon, B.G., Chiu, L.N.S., Price, M.: Predicting low velocity impact damage and Compression-after-impact (CAI) behaviour of composite laminates. Compos. Part A: Appl. Sci. Manufac. **71**, 212–226 (2015)
44. Tan, W., Falzon, B.G.: Modelling the crush behaviour of thermoplastic composites. Compos. Sci. Technol. **134**, 57–71 (2016)
45. Falzon, B.G.: Computational modelling of the crushing of carbon fibre-reinforced polymer composites. Philosophical Trans. Royal Soc. **A 380**, 20210336 (2022)
46. Dear, J.P., MacGillivray, J.H.: Strain gauging for accurate determination of K and G in impact tests. J. Mater. Sci. **26**, 2124–2132 (1991)
47. Crouch, B.A., Williams, J.G.: Modelling of dynamic crack propagation behaviour in the three-point bend impact specimen. J. Mech. Phys. Solids **36**, 1–13 (1988)
48. Williams, J.G., Adams, G.C.: The analysis of instrumented impact tests using a mass-spring model. Int. J. Fract. **33**, 209–222 (1987)
49. Dear, J.P.: High speed photography of impact effects in the three-point bend testing of polymers. J. Appl. Phys. **67**, 4304–4312 (1990)

Publisher's Note Springer Nature remains neutral with regard to jurisdictional claims in published maps and institutional affiliations.